JOURNAL OF SYNCHROTRON RADIATION
ISSN 1600-5775

Received 11 December 2015
Accepted 16 May 2016

Edited by A. F. Craievich, University of São Paulo, Brazil

Keywords: X-ray nanotomography; scanning electron microscopy; quantitative image analysis; three-dimensional reconstruction; nanocomposite powder.

X-ray nanotomography and focused-ion-beam sectioning for quantitative three-dimensional analysis of nanocomposites

Christopher E. Shuck,[a] Mathew Frazee,[b] Andrew Gillman,[b] Matthew T. Beason,[c] Ibrahim Emre Gunduz,[c] Karel Matouš,[b] Robert Winarski[d] and Alexander S. Mukasyan[a]*

[a]Department of Chemical and Biomolecular Engineering, University of Notre Dame, Notre Dame, IN 46556, USA, [b]Department of Aerospace and Mechanical Engineering, University of Notre Dame, Notre Dame, IN 46556, USA, [c]School of Mechanical Engineering, Purdue University, West Lafayette, IN 47907, USA, and [d]Center for Nanoscale Materials, Argonne National Laboratory, Argonne, IL 60439, USA. *Correspondence e-mail: amoukasi@nd.edu

Knowing the relationship between three-dimensional structure and properties is paramount for complete understanding of material behavior. In this work, the internal nanostructure of micrometer-size (~10 μm) composite Ni/Al particles was analyzed using two different approaches. The first technique, synchrotron-based X-ray nanotomography, is a nondestructive method that can attain resolutions of tens of nanometers. The second is a destructive technique with sub-nanometer resolution utilizing scanning electron microscopy combined with an ion beam and 'slice and view' analysis, where the sample is repeatedly milled and imaged. The obtained results suggest that both techniques allow for an accurate characterization of the larger-scale structures, while differences exist in the characterization of the smallest features. Using the Monte Carlo method, the effective resolution of the X-ray nanotomography technique was determined to be ~48 nm, while focused-ion-beam sectioning with 'slice and view' analysis was ~5 nm.

1. Introduction

A material's behavior in response to external stimuli, whether mechanical, chemical, electrical or otherwise, is strongly coupled to its bulk structural characteristics (Espinosa *et al.*, 2012; Nachtrab *et al.*, 2011; Gillman *et al.*, 2013, 2015; Liu *et al.*, 2015; Torquato, 2002; Gillman & Matouš, 2014). As the structure of the material becomes finer, approaching the nanometer-size range, it becomes increasingly difficult to develop techniques that can characterize morphology statistically and accurately, yet it is often critical to predicting macroscopic response. Indeed, it is well known that materials, as they reach nanometer length-scales, often exhibit drastically different effective properties than their bulk counterparts (Alloyeau *et al.*, 2009; Roduner, 2006; Wang *et al.*, 2006; Baldi *et al.*, 2014). The increasing use of nano-materials necessitates further development of advanced imaging and characterization techniques that allows valid data on their internal three-dimensional (3D) structural characteristics to be obtained.

Several techniques have been developed that permit examination of material structures on nano or even atomic size scales, including scanning tunneling microscopy (STM) and transmission electron microscopy (TEM). These techniques have proven to be extremely valuable in the characterization and understanding of materials and their properties. However, one significant drawback of these techniques is that

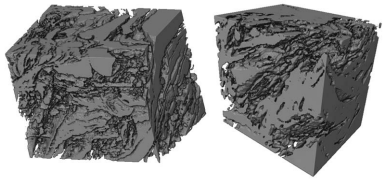

they are limited to two-dimensional (2D) analysis for the majority of samples; when the samples are adequately thinner, 3D studies become possible. In both cases, however, only a small amount of material can be analyzed. Moreover, this limited volume may or may not be representative of the entire material domain. Therefore, it is critical to characterize a large material volume in order to reduce sampling bias that is inherent in other techniques.

X-ray nanotomography (XRnT) works by passing high-brilliance X-rays through a sample. The sample absorbs a fraction of the X-rays; the transmission rate is functionally dependent on the average atomic number of the phases (Withers, 2007; Nugent *et al.*, 1996). Because of this, contrast between different material phases can be imaged, where each phase absorbs a different fraction of X-rays. In order to convert this 2D projection into three dimensions, the sample is rotated and the same quality of X-rays are passed through again and the projections at different angles are collected; this collection of images can be combined, leading to a 3D map of the internal sample (Withers, 2007). The 'slice and view' (S&V) technique is conducted with scanning electron microscopy (SEM) and focused ion beam (FIB) (Uchic *et al.*, 2006). An image is taken using SEM, then a layer of known thickness is milled away by FIB, then another image is taken. This is repeated multiple times with use of the S&V software. Contrast between different phases in this technique can be accomplished by using either a backscattering detector or a secondary electron detector. Again, the obtained set of images can be reconstructed, leading to the phase distributions along the bulk of the sample (Uchic *et al.*, 2006).

High-energy ball milling (HEBM) is a well known technique for enhancing the reactivity of solid phase reactants through modification of the microscale features (Takacs, 2002; Dreizin, 2009; Shteinberg *et al.*, 2010). HEBM significantly reduces the reaction onset temperature with increased combustion characteristics (Rogachev & Mukasyan, 2010; Rogachev *et al.*, 2013; Manukyan *et al.*, 2013, 2015; Shuck *et al.*, 2016). These reactive nanocomposites have many applications, including in explosives, propellants, pyrotechnics and materials synthesis (Mukasyan *et al.*, 2015). This technique takes single-phase reactant powders and combines them into microscale particles with nanoscale geometric features that contain all reactant phases with oxide-free boundaries. The structure of these particles is quite complicated; HEBM results in inhomogeneous, tortuous, stochastic structures that have features with varying size scales, from 10 nm to 10 μm in some cases. Due to the complexity of the internal structure, HEBM-produced particles are ideal for testing the limits of 3D processing techniques.

In this article, data are collected from HEBM-composite particles under identical processing conditions by both XRnT and S&V approaches. The data require unique reconstruction steps, while quantitative analysis of the 3D dataset is the same. A comparison of data collection times and resolution between the two techniques is conducted. Finally, the results of the two techniques are compared, with focus being placed on X-ray nanotomography.

2. Methodology

2.1. Initial reactant synthesis

In this study, we used mechanically induced Ni/Al nanocomposite particles as a model system. HEBM was performed using a PM100 (Retsch, Germany) planetary ball mill in a 250 ml steel jar with 10 mm balls of the same material. The jar was filled with 99.999% pure argon. The ball-to-powder ratio was 5:1. A rotational speed of 650 r.p.m. was used, with the internal sun wheel rotation speed being 1300 r.p.m. For each treatment, 35 g of an equiatomic (1:1) mixture of Ni (Alfa Aesar; 3–7 μm) + Al (Alfa Aesar; 7–15 μm) was subjected to wet grinding in hexane for a total duration of 30 min, which consisted of six 5 min periods of milling, each followed by 60 min of cooling. The resulting powder was sieved, and fabricated composite particles with average size in the range 10–20 μm were selected for further analysis.

2.2. Data collection

The two techniques were used for data collection on the nano-structural characteristics of the composite particles, *i.e.* S&V method by scanning electron microscopy/focused ion beam (SEM/FIB) and XRnT. For both cases, ten different random particles from the same synthesis batch were chosen for analysis.

A Nanolab 600 Helios Dual SEM/FIB (FEI, USA) was used for obtaining cross-sectional images through the FIB/SEM approach. The electron microscope was equipped with a backscattering detector. The S&V software package was used to collect a set of ∼500 images per particle with ∼10 μm width, ∼10 μm depth and ∼5 nm pixel size with a voltage of 30 kV and with a milling current of 9.7 pA. These images were taken in series after milling 10 nm in between each frame, leading to an analyzed volume of ∼500 μm^3. Considering all particles analyzed, a total volume of ∼2000 μm^3 was prepared for further structural analysis.

For the nanotomography approach, particles were welded onto thin (0.5 μm) tungsten needles. Collection of XRnT data was conducted at the Hard X-ray Nanoprobe beamline (Sector 26) operated by the Center for Nanoscale Materials and the Advanced Photon Source at Argonne National Laboratory. The setup is described in great detail elsewhere (Winarski *et al.*, 2012; Holt *et al.*, 2013). Briefly, 2D projection images were collected with an initial exposure time of 2 s, with source energy of 8345 eV, and pixel size of 11.8 nm, with 12 μm field of view; a 80 μm diameter, 300 nm thickness, 24 nm outermost zone-width zone plate was utilized. This optic has an efficiency of about 0.5%. To provide 3D sets of data, the particles were rotated with steps of 1°, 0.25° or 0.1° in between images, which corresponds to 180, 720 or 1800 images per particle, respectively.

2.3. 3D reconstruction and image processing

After acquisition of images, both techniques required reconstruction of the raw data in order to form a 3D data set. 3D reconstruction of the cross-sectional images collected with

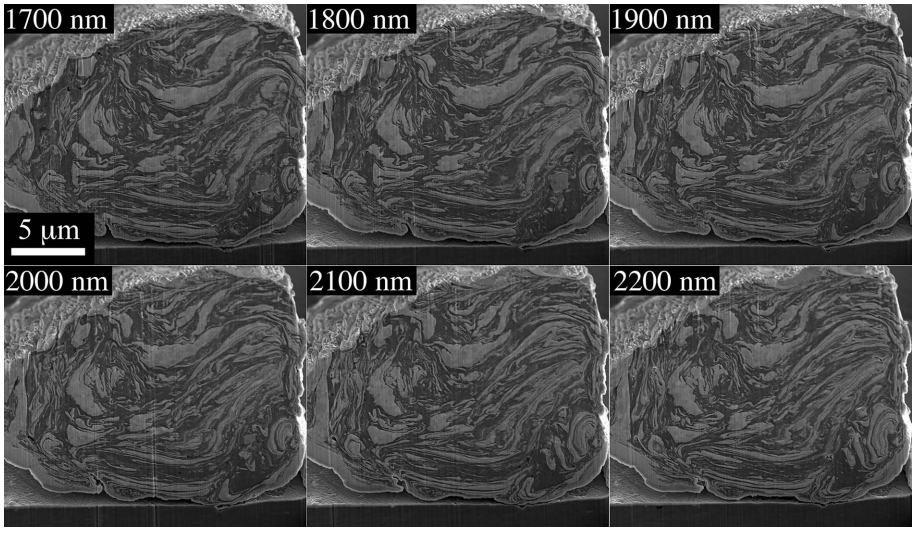

Figure 1
Raw cross-sectional images 100 nm apart obtained from FIB S&V (Ni is the brighter phase, Al is the darker phase).

the FIB/SEM approach (Fig. 1) was completed using the *AvizoFire* (FEI) software package. The series of images collected from the FIB S&V were first shear corrected (38°) in the *y* direction, contrast normalized and then aligned using a least-squares method. After alignment, in order to remove the edge artifacts (deposited platinum, particle edges and steel support stub), the internal volume of the particle was extracted.

For the frames obtained using the nanotomography approach, the *TXM Wizard* software package was used first in order to align the images (Liu *et al.*, 2012). Each individual projection image underwent background subtraction; this ensured that all pixel intensities were representative of X-ray attenuation through the sample. The grayscale values were inverted, leading to nickel being the brighter phase and aluminium the darker phase. Following background reference correction, alignment of the sample about its rotational axis was necessary due to microscale mechanical jitter that occurs when rotating the particle. The first part of the alignment process involved marking a common feature on the sample that is visible from all projection angles, which is used as a fiducial. After marking the reference point on each projection image, further automatic alignment refining can be performed. Two alignment procedures were used for the analysis, *i.e.* a cross-correlation alignment (CCA) algorithm and a scale invariant feature transform algorithm (Liu *et al.*, 2012). Given the nature of the nanocomposite Ni/Al particles, it was found that the CCA algorithm is more effective at aligning the rotational axis of the sample, due to its more holistic approach that compares a much larger amount of pixel intensities in each projection image and shifts the image according to the location of greatest correlation.

After attaining sufficient sample alignment, a new set of projection images that are dynamically cropped such that the rotational axis remains in a constant position is created. This new aligned image stack is then reconstructed using *TXM Wizard*. The preferred reconstruction algorithm for these samples is the filtered back-projection method, as it provided the same pixel density and similar intra-particle image quality as the alternative Algebraic Reconstruction Technique (ART), while being significantly less computationally expensive [*O* (hours) compared with *O* (days)] (Liu *et al.*, 2012). A comparison of two corresponding cross sections of a given sample is shown in Fig. 2. Note that the ART algorithm results in less noise in the air space. However, when comparing the quality of the internal volume of the composite particles, the quality is similar.

After reconstruction of the 3D datasets from both imaging methods, *AvizoFire*'s image processing algorithms are utilized to identify the material phase of interest and quantify the local structural features. Initially, the reactants were isolated by use of contrast thresholding. Since the materials examined in this work are composed of only two components (Figs. 1 and 3*a*: Al is the darker phase and Ni is the brighter phase), in order to separate the respective material phases for quantitative analysis the gray level image is binarized (see Fig. 3*b*). Each of the phases (Ni and Al) has a distribution of grayscale values within the phases themselves due to the difference in signal (*Z*-contrast and density contrast) that occurs during data collection for both techniques. These ranges only partially overlap, which results in a grayscale minimum, which is selected for best separation of the phase (Gillman *et al.*, 2013). In order to quantitatively obtain information about the nanostructural characteristics of the nanocomposites, 3D skeletonization using a distance-ordered thinner was also utilized (see Fig. 3*c*). The distance-ordered thinning method is often described as an 'onion peeling' method, since it strips off the outer boundary layers then checks to ensure that the criteria is met before removing another layer (Pudney, 1998). Formally,

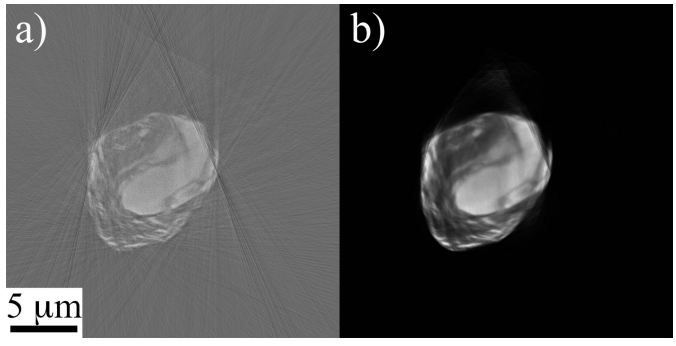

Figure 2
Comparison of algorithms for reconstructing nanotomography projection images. Cross section from 3D dataset using the (*a*) filtered-back-projection and (*b*) algebraic-reconstruction technique.

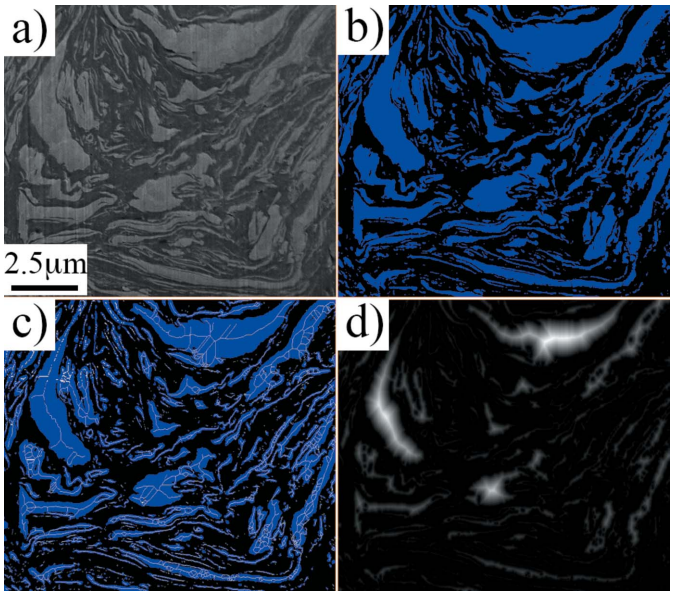

Figure 3
Pipeline used for quantitative 3D reconstruction showing (*a*) raw data, (*b*) phase isolation by thresholding, (*c*) distance-ordered thinning leading to skeleton of the structure, and (*d*) chamfer distance map showing the distance of each voxel from the other phase.

this algorithm thins the foreground objects, while preserving the topology; this results in thin homotopic skeletons (Pudney, 1998). 3D chamfer distance mapping was used for determining the distances of each voxel to the nearest voxel of opposite composition (Fig. 3*d*). Finally, the skeleton is multiplied by the distance map, which provides a measure of the half-thickness for each segment of the structure.

In addition to quantifying the local thicknesses in the structures, *n*-point probability functions are computed using the in-house Monte Carlo sampling code *Stat3D* (Lee *et al.*, 2009; Gillman *et al.*, 2013, 2015; Gillman & Matouš, 2014). In this work, one- and two-point probability functions are computed directly from the thresholded data set (see Fig. 3*b*). This function characterizes the spatial arrangement of the constituent and quantifies both the short- and long-range character.

3. Results

Raw data from FIB S&V are shown in Fig. 1, where each image was taken 100 nm apart from the preceding one. The pixel size of the electron microscopy image is determined by the selected magnification. For these specific experiments, an (x,y) pixel size of $\sim$5 nm was used. However, it is possible to have higher resolutions if necessary; for this system the maximum attainable resolution is 0.9 nm. Because the pixel size in the z-direction was 10 nm, this method is anisotropic. The corresponding raw data from XRnT are shown in Fig. 4; each of the images are 30° apart, depicting a representative set of angles around the entire particle. These data represent the transmission of X-rays through the complete volume of the sample. In these images, again the brighter phase is Ni and the darker phase is Al. The observed various grayscale intensities are due to both particle thickness variation and elemental composition. For the data processed through XRnT, all reconstructed samples attained a perfectly cubic voxel size of 11.8 nm, which corresponds to the pixel size of the optics utilized in data collection.

The time of data collection for both FIB S&V and for XRnT linearly increases with the number of images. For FIB S&V, depending on the size of each slice, it takes 30–60 s per image, including milling and image acquisition. For the samples described above, the total acquisition of 500 μm^3 data took $\sim$480 min. If a higher resolution is required for FIB S&V, the acquisition time to collect an appropriate volume increases. As the resolution increases, the cross-sectional area imaged per image decreases correspondingly. For XRnT, each image, with the settings selected to optimize the contrast in the Ni/Al system, took $\sim$7 s. For capturing the highest resolution (1800 images) of a particle with total volume $\sim$375 μm^3, the total acquisition time was $\sim$175 min. The data acquisition times in both cases do not take into account sample preparation or any preliminary equipment setup.

A qualitative comparison of the data, represented by the rendering of the Ni phase (void space represents the Al phase), obtained from both techniques is shown in Fig. 5. In the FIB S&V data, the complete volume is represented by a bounding box that eliminates the outer edges of the particle and the deposited Pt-layer. Although the XRnT data are also

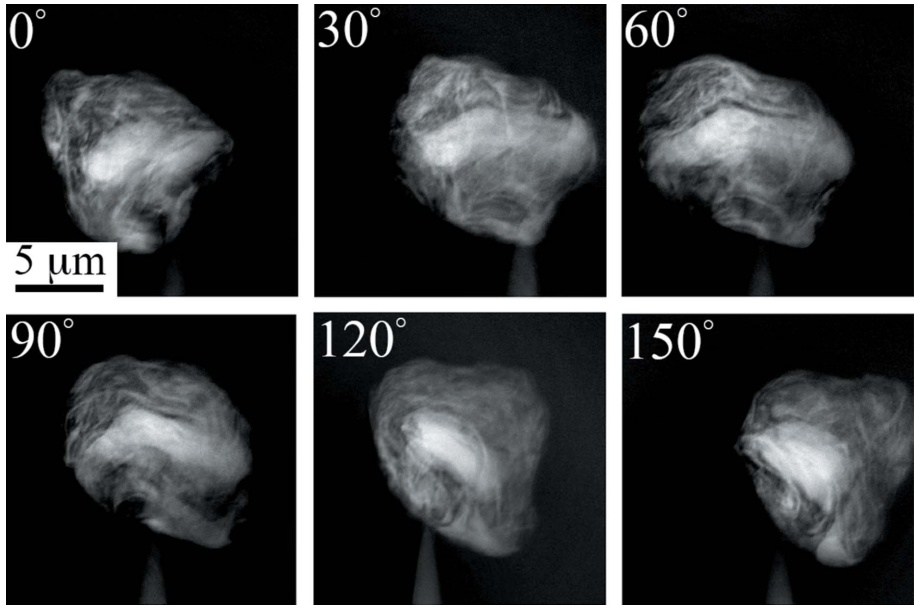

Figure 4
Projection images obtained from the nanotomography technique.

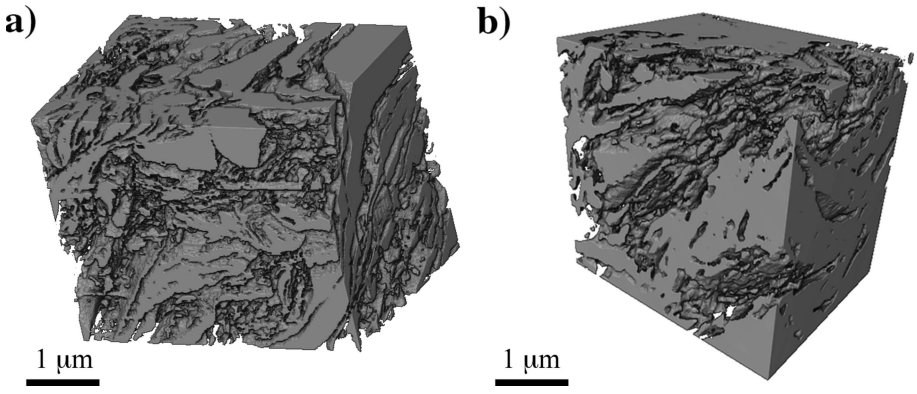

Figure 5
Volume renderings of thresholded Ni phase for data obtained from (*a*) FIB S&V and (*b*) X-ray nanotomography.

shown as a bounding box, this is not required by the technique when using the ART reconstruction algorithm. The complete volume of the particle can be analyzed.

It can be seen that the two sets of data appear to have qualitatively similar amounts of tortuosity and general structural inhomogeneity. However, in the XRnT reconstruction, the structures appear to be more rounded. There are instances in the XRnT sample where two or more layers are smeared together, resulting in larger apparent features. In the FIB S&V reconstruction, the layers are more sharply defined, and the structures appear to be less rounded and uniform. Even the smallest observed layers have sharp interface boundaries and are multiple pixels thick, which indicates that the effective resolution for the FIB S&V method is high enough to capture all of the smallest features that are present in the sample.

The layer thickness distributions obtained by using both techniques are shown in Fig. 6. It can be seen in Fig. 6(*a*) that X-ray nanotomography characterization results in a higher average Al thickness (1012 nm *versus* 715 nm for FIB S&V), along with slightly different distributions thereof. The XRnT distribution is shifted to a higher average and is broader; the corresponding right end of the tail proceeds farther by ∼500 nm. For analysis of nickel (Fig. 6*b*), the average thickness is again larger (∼15%) for XRnT, 1394 nm compared with 1178 nm for FIB S&V. Additionally, the Ni distributions, while similar, are slightly broader for XRnT. Finally, the XRnT shows a larger standard deviation (σ) for both Ni and Al distributions (1006 nm and 535 nm), as compared with those for FIB S&V (761 nm and 387 nm, respectively).

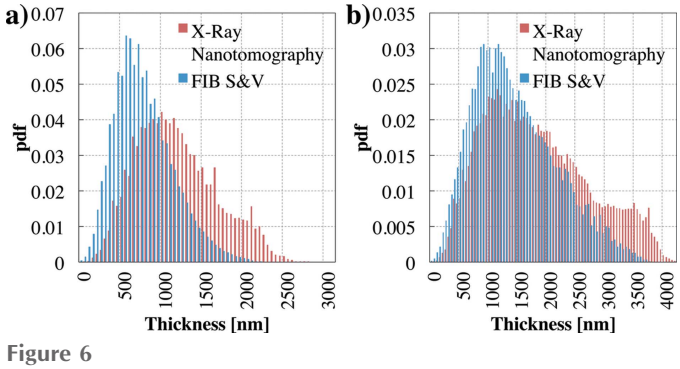

Figure 6
Average thickness distributions computed using the image processing pipeline for (*a*) Al and (*b*) Ni phases. The resulting distributions from both FIB/S&V and X-ray nanotomography characterization techniques are compared.

The isotropic two-point probability function $S_{\mathrm{Al,Al}}(r)$ for one particle of each imaging method is computed using *Stat3D* and is shown in Fig. 7. This function represents the probability of finding two points separated by a distance r in Al. At the origin ($r = 0$), the functions degenerate to the volume fraction of Al, c_{Al}. For homogeneous and ergodic systems, the function saturates to the volume fraction squared as r approaches infinity (red dash-dotted line). The function for the FIB S&V data (solid black line) saturates at the expected value, while the function for nanotomography (dashed blue line) does not. Given the random nature of the microstructures observed, the behavior of this function provides a measure for determining the amount of volume necessary to fully capture the long-range order. Furthermore, the saturation point of these functions has shown to be a good measure for creating representative computational domains for modeling effective material response (Mosby & Matouš, 2015).

4. Discussion

The broadening of the X-ray nanotomography distributions (Fig. 6), as well as the discussed features of the reconstructed images (Fig. 5), indicates that although the optics used in these experiments have a pixel size of 11.8 nm, we were not able to reach this level of resolution in the reconstructed media. The smearing effect shifts and broadens the thickness distributions for both Ni and Al phases.

In order to determine what the real resolution is, a Monte Carlo (MC) algorithm (see Algorithm 1 below) was utilized that takes the data obtained from the FIB S&V and smears the smallest layers in ascending order to simulate the distributions obtained by XRnT.

Algorithm 1: Monte Carlo Procedure
Evaluate average thickness (F_{AVG}) of FIB thickness distribution (F)
Evaluate average thickness (X_{AVG}) of X-ray Nanotomography data
while $F_{AVG} < X_{AVG}$
  Subtract one count from smallest histogram bin, L_{MIN}, of F
  Select a layer thickness (L_1) at random from F
  Subtract one count from histogram bin containing L_1
  Add one count to the bin in F containing $2*L_1$
  Compute new F_{AVG}
end while

This MC method was run multiple times, showing that the smallest remaining layer thickness [L_{MIN} of modified FIB

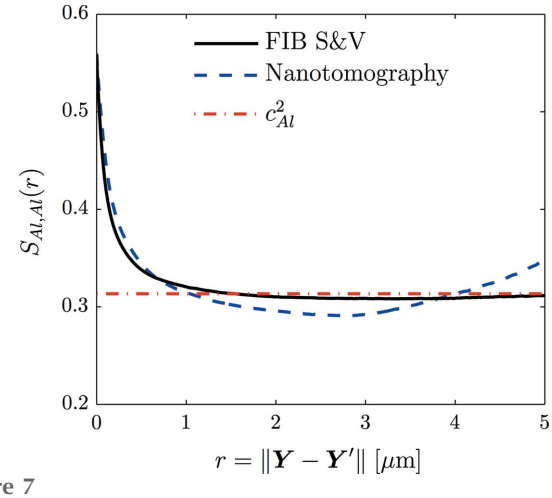

Figure 7
Two-point probability function, $S_{\mathrm{Al,Al}}(r)$, of the aluminium phase from FIB S&V and X-ray nanotomography datasets. The functions are compared with the value of the square of the Al volume fraction, c_{Al}^2.

thickness distribution (F)], and consequent effective pixel size, is ∼48 nm. This resolution can be improved by better mechanical control of the sample coupled with more robust alignment algorithms. Indeed, the initial alignment of the sample is very challenging when using smaller samples, and artifacts during processing are difficult to eliminate; a single misaligned frame can significantly degrade the accuracy of the reconstruction and the remaining image processing steps. Controlling the sample to keep the entire particle in focus is difficult, even with state-of-the-art mechanical control; multiple data acquisition runs are rendered useless due to micrometer-length movement of the holding mechanism. The difficulty of perfect alignment and validation thereof combined with a lower resolution results in nano-features being 'smeared'.

However, the resolution is not the only factor that needs to be considered for these techniques. The amount of volume that can be analyzed by each method is critical for accurate quantification of the long-range structures, as illustrated in Fig. 7. From this higher-order statistical analysis, only the FIB S&V two-point probability function approaches c_{Al}^2. Note that the largest dimensions of the thresholded datasets analyzed are approximately 10 µm and 5 µm for FIB S&V and nanotomography data, respectively, and that the mechanical control issue described above limits the size of the nanotomography domain considered. Therefore, only the FIB S&V technique is able to characterize large enough volumes for capturing both local, *e.g.* average layer thickness, and long-range character.

Despite its limitations, X-ray nanotomography is currently the preferred nondestructive technique for characterization of the internal structure of the materials. This leads to the possibility of directly comparing structures before and after external stimuli (shock, ignition, *etc.*), which is impossible with any other techniques, including FIB S&V. Also, XRnT can be accomplished in air, while FIB S&V requires high vacuum. Thus, XRnT makes it possible to study samples that degrade in vacuum. Studies need not be limited to simply air; one can utilize differing temperatures, pressures and chemical environments with relative ease. Additionally, samples that are sensitive to electron beams can instead be studied with X-rays. This technique can also be used to examine large, thick samples (Holt *et al.*, 2013), which is not easily feasible with other methods. Finally, as was mentioned above, the XRnT allows characterization of the entire volume of the sample; there is no need to eliminate the outer particle volume from analysis, as with other techniques. The use of higher-order statistics (Fig. 7) has shown that the volumes obtained are insufficient for describing long-range character. It is imperative that users of these techniques consider this limitation; otherwise conclusions drawn from the data may not accurately represent the physics that is present.

FIB S&V, while used as the method of comparison with XRnT, does have its own limitations and drawbacks, as do all techniques. The resolution of data collection nonlinearly scales with time: as increasingly finer resolutions are required, the acquisition times increases rapidly. The resulting voxel size for samples will be anisotropic, often in all three dimensions. Layer milling may be inaccurate due to sample drift, leading to uneven slices in the z-direction. Finally, backscattering data may be smeared due to the penetration depth of electrons.

5. Conclusions

Techniques such as XRnT and FIB-assisted sectioning in conjunction with 3D reconstruction software packages enable characterization, and consequent understanding, of complicated 3D structures with nanoscale resolution. The purpose of this work is to establish a methodology for accurate characterization of HEBM-produced metallic nanocomposite materials by use of these techniques. This leads to a new paradigm for material science, where quantitative trends between observed 3D structures and their properties can be developed. In particular, the structural characterization of HEBM composite particles considered in this work allows us to improve modeling and understanding of the multiphysics phenomena in material synthesis and high energy density applications.

We have shown that X-ray nanotomography is a technique that offers significant benefits for characterization of nanostructured metallic composites. It fulfills a role for nondestructive 3D characterization of samples with sufficient accuracy in a short period (minutes) of time. This is critical for further experiments where the same, already characterized, particles are used. We have determined that the utilized experimental setup offers 11.8 nm pixel size of the optics, and ∼48 nm effective resolution after reconstruction; however, there is room for enhancement of the latter parameter with improvements to the rotating stage. Overall, the ability of research groups to access synchrotron facilities is incredibly valuable; accurate, reliable characterization of nanomaterials is key to fundamental understanding and progress as a whole. However, care must be taken to ensure that convergence of

the data is reached, measured through rigorous statistical analysis.

Acknowledgements

This work was supported by the Department of Energy, National Nuclear Security Administration, under Award Number DE-NA0002377 as part of the Predictive Science Academic Alliance Program II. Funding from the Defense Threat Reduction Agency (DTRA), Grant Number HDTRA1-10-1-0119. Counter-WMD basic research program, Dr Suhithi M. Peiris, Program Director, is also gratefully acknowledged. Funding from the National Defense Science and Engineering Graduate Fellowship is acknowledged. Use of the Center for Nanoscale Materials and the Advanced Photon Source, both Office of Science user facilities, was supported by the US Department of Energy, Office of Science, Office of Basic Energy Sciences, under Contract No. DE-AC02-06CH11357.

References

Alloyeau, D., Ricolleau, C., Mottet, C., Oikawa, T., Langlois, C., Le Bouar, Y., Braidy, N. & Loiseau, A. (2009). *Nat. Mater.* **8**, 940–946.
Baldi, A., Narayan, T. C., Koh, A. L. & Dionne, J. A. (2014). *Nat. Mater.* **13**, 1143–1148.
Dreizin, E. L. (2009). *Prog. Energy Combust. Sci.* **35**, 141–167.
Espinosa, H. D., Bernal, R. A. & Filleter, T. (2012). *Small*, **8**, 3233–3252.
Gillman, A., Amadio, G., Matouš, K. & Jackson, T. (2015). *Proc. R. Soc. London A*, **471**, 20150060.
Gillman, A. & Matouš, K. (2014). *Phys. Lett. A*, **378**, 3070–3073.
Gillman, A., Matouš, K. & Atkinson, S. (2013). *Phys. Rev. E*, **87**, 022208.
Holt, M., Harder, R., Winarski, R. & Rose, V. (2013). *Annu. Rev. Mater. Res.* **43**, 183–211.
Lee, H., Brandyberry, M., Tudor, A. & Matouš, K. (2009). *Phys. Rev. E*, **80**, 061301.
Liu, Q., Li, X., Xiao, Z., Zhou, Y., Chen, H., Khalil, A., Xiang, T., Xu, J., Chu, W., Wu, X., Yang, J., Wang, C., Xiong, Y., Jin, C., Ajayan, P. M. & Song, L. (2015). *Adv. Mater.* **27**, 4837–4844.
Liu, Y., Meirer, F., Williams, P. A., Wang, J., Andrews, J. C. & Pianetta, P. (2012). *J. Synchrotron Rad.* **19**, 281–287.
Manukyan, K. V., Lin, Y., Rouvimov, S., McGinn, P. J. & Mukasyan, A. S. (2013). *J. Appl. Phys.* **113**, 024302.
Manukyan, K. V., Shuck, C. E., Rogachev, A. S. & Mukasyan, A. S. (2015). *J. Vis. Exp.* **98**, e52624.
Mosby, M. & Matouš, K. (2015). *Modell. Simul. Mater. Sci. Eng.* **23**, 085014.
Mukasyan, A. S., Rogachev, A. S. & Aruna, S. T. (2015). *Adv. Powder Technol.* **26**, 954–976.
Nachtrab, S., Kapfer, S. C., Arns, C. H., Madadi, M., Mecke, K. & Schröder-Turk, G. E. (2011). *Adv. Mater.* **23**, 2633–2637.
Nugent, K. A., Gureyev, T. E., Cookson, D. F., Paganin, D. & Barnea, Z. (1996). *Phys. Rev. Lett.* **77**, 2961–2964.
Pudney, C. (1998). *Comput. Vis. Image Underst.* **72**, 404–413.
Roduner, E. (2006). *Chem. Soc. Rev.* **35**, 583–592.
Rogachev, A. S. & Mukasyan, A. S. (2010). *Shock Waves*, **46**, 243–266.
Rogachev, A. S., Shkodich, N. F., Vadchenko, S. G., Baras, F., Kovalev, D. Y., Rouvimov, S., Nepapushev, A. A. & Mukasyan, A. S. (2013). *J. Alloys Compd.* **577**, 600–605.
Shteinberg, A. S., Lin, Y., Son, S. F. & Mukasyan, A. S. (2010). *J. Phys. Chem. A*, **114**, 6111–6116.
Shuck, C. E., Manukyan, K. V., Rouvimov, S., Rogachev, A. S. & Mukasyan, A. S. (2016). *Combust. Flame*, **163**, 487–493.
Takacs, L. (2002). *Prog. Mater. Sci.* **47**, 355–414.
Torquato, S. (2002). *Random Heterogeneous Materials.* New York: Springer-Verlag.
Uchic, M. D., Groeber, M. A., Dimiduk, D. M. & Simmons, J. P. (2006). *Scr. Mater.* **55**, 23–28.
Wang, X. W., Fei, G. T., Zheng, K., Jin, Z. & Zhang, L. D. (2006). *Appl. Phys. Lett.* **88**, 173114.
Winarski, R. P., Holt, M. V., Rose, V., Fuesz, P., Carbaugh, D., Benson, C., Shu, D., Kline, D., Stephenson, G. B., McNulty, I. & Maser, J. (2012). *J. Synchrotron Rad.* **19**, 1056–1060.
Withers, P. J. (2007). *Mater. Today*, **10**, 26–34.